HgTe Nanocrystals for SWIR Detection and their Integration up to Focal Plane Array

Audrey Chu, Bertille Martinez, Simon Ferré, Vincent Noguier, Charlie Gréboval, Clément Livache, Junling Qu, Yoann Prado, Nicolas Casaretto, Nicolas Goubet, et al.

HgTe Nanocrystals for SWIR Detection and their Integration up to Focal Plane Array

Audrey Chu[1,2], Bertille Martinez[1,3], Simon Ferre[4], Vincent Noguier[4], Charlie Gréboval[1], Clément Livache[1,3], Junling Qu[1], Yoann Prado[1], Nicolas Casaretto[1], Nicolas Goubet[1,5], Hervé Cruguel[1], Lenart Dudy[6], Mathieu G. Silly[6], Grégory Vincent[2], Emmanuel Lhuillier[1*]

[1]Sorbonne Université, CNRS, Institut des NanoSciences de Paris, INSP, F-75005 Paris, France

[2] ONERA-The French Aerospace Lab, Chemin de la Hunière, BP 80100, F-91123 Palaiseau, France

[3]Laboratoire de Physique et d'Étude des Matériaux, ESPCI Paris PSL Research University, Sorbonne Université Univ Paris 06, CNRS, 10 rue Vauquelin 75005 Paris, France.

[4]New Imaging Technologies SA, 1 impasse de la Noisette 91370 Verrières le Buisson, France

[5] Sorbonne Université, CNRS, De la Molécule aux Nano-objets: Réactivité, Interactions et Spectroscopies, MONARIS, F-75005 Paris, France

[6]Synchrotron-SOLEIL, Saint-Aubin, BP48, F91192 Gif sur Yvette Cedex, France

Abstract: Infrared applications remain too often a niche market due to their prohibitive cost. Nanocrystals offer an interesting alternative to reach cost disruption especially in the shortwave infrared (SWIR, λ<1.7 µm) where material maturity is now high. Two families of materials are candidate for SWIR photoconduction: lead and mercury chalcogenides. Lead sulfide typically benefits from all the development made for wider bap gap such as the one made for solar cells, while HgTe takes advantage of development relative to mid wave infrared detector. Here we make a fair comparison of the two material detection properties in the SWIR and discuss the material stability. At such wavelengths, studies have been mostly focused on PbS rather than on HgTe, therefore we focus in the last part of the discussion on the effect of surface chemistry on the electronic spectrum of HgTe nanocrystals. We unveil that tuning the capping ligands is a viable strategy to adjust the material from p-type to ambipolar. Finally, HgTe nanocrystals are integrated into multi pixel devices to quantize spatial homogeneity and onto read out circuits to obtain fast and sensitive infrared laser beam profile.

Keywords: nanocrystals, infrared detection, focal plane array, short wave infrared, HgTe.

INTRODUCTION

The ease to tune the optical features of nanocrystals is certainly one of their most striking properties. By combining quantum confinement with the broad list of materials which can be synthetized under colloidal nanoparticle form, the energy of the optical transition can be tuned from a few meV[1] (far IR) up to several eV (UV). Quickly after the discovery of their light emission properties in the visible range, the possibility to reach infrared wavelengths[2] has become one of the most promising applications of inorganic nanocrystals and a key advantage compared to organic materials. Infrared applications of nanocrystals have first been focused on the harvesting of the infrared part of the solar spectrum for solar cell applications[3]. Later, their potential for the design of infrared detectors[4,5] has also been explored in various ranges of wavelengths from near infrared (NIR, ≈1 µm)[6–8], short wave infrared (SWIR, <1.7 µm)[9–11], extended short wave infrared (ESWIR, <3 µm)[12–16], mid wave infrared (MWIR, 3-5 µm)[17–20] to even long wave infrared (LWIR, 8-12 µm)[21,22].

The cost of an infrared sensor can be split over three parts: (i) the active material, meaning the substrate and the grown semiconductor layer absorbing in the infrared, (ii) the cooling machine which become mandatory for thermal imaging and (iii) the packaging (*i.e.* the optics and surrounding electronics of the active layer). Reaching low-cost devices cannot address only one of these parts. Thus, it is unlikely to design a low cost device with a cryogenic operating temperature[23]. As a result, it appears that low cost devices are more likely to be obtained in the SWIR range: indeed the band gap is large compared to the thermal energy which reduces the thermally activated carrier density. Currently the detection in the SWIR is driven by InGaAs technology. The InGaAs layer is grown using MBE (molecular beam epitaxy) on an InP substrate and achieve high performances[24]: dark current density in the nA.cm^{-2}, small pixel pitch down to 15 µm and an external quantum efficiency around 80%. On the other hand, the technology which is highly mature has limited cost disruption perspectives. It also suffers from a lack of spectral tunability. In particular, the device cannot be used in the visible range due to the InP substrate absorption and its tunability toward longer wavelengths is also difficult. The targeted detection wavelength in the infrared makes that it is also unlikely that organic electronics may offer a viable alternative to InGaAs. On the other hand, nanocrystals can offer such an alternative. The field is currently boosted by interest for perovskites materials[25,26], but their band gaps remain too large to be operated in the SWIR range. Two materials appear as potential candidates: lead chalcogenides and mercury chalcogenides, see Figure 1a. Lead chalcogenides have been widely used in the NIR for solar cells. In this case, small nanocrystals (3-4 nm) are used. To reach the SWIR range[27,28], larger nanocrystals around 8 nm are necessary. Such sizes are nevertheless acceptable to obtain colloidally stable solutions. Alternatively, HgTe nanocrystals have been widely investigated in the recent years[29–31] for longer wave applications in the extended SWIR[9,12,14,16] and MWIR[18] ranges. To reach the SWIR range with HgTe[32,33] smaller nanocrystals[31] (*i.e.* with more confinement) than the one used for MIWR have to be grown. Alternatively a ternary alloy with Cd[34,35] can be synthetized. However, in the latter case very small Cd content needs to be introduced which generates difficulties to finely reproduce the band gap from batch to batch.

In this paper, we grow nanoparticles with a bandgap similar to InGaAs' one and make a comparison of the potential of PbS and HgTe as InGaAs alternative. While many reports already dealt with photoconduction of narrow band gap nanocrystals in the SWIR, many critical issues remain pushed under the rug. In particular, while an important effort has been conducted to determine the electronic spectrum of PbS[36] with a solar cell compatible band gap (950 nm), such effort still lacks in the SWIR, especially for HgTe. Here we determine, the exact nature of the majority carriers, the origin of the degradation mechanism under annealing and the tunability of the bands depending on the ligands. Addressing these questions is a mandatory step toward the integration of the nanocrystals into commercial devices. The last part of the discussion is dedicated to the integration of the material into multipixel devices and focal plane arrays to quantize their potential for imaging.

DISCUSSION

We first start by synthetizing HgTe and PbS nanocrystals with a cut-off wavelength equal to 1.7 µm. This actually nicely matches the cut-off of InGaAs detector, see Figure 1b. HgTe and PbS nanocrystals are respectively synthetized using the Keuleyan's[37] and Moreels'[38] procedures, see methods. As HgTe is a semimetal, the energy of the interband transition is purely due to quantum confinement. This induces that small nanoparticles are grown to reach SWIR range. They have rod-like shape with a length around 8nm and a diameter of 3 nm, see Figure 1c. PbS is a semiconductor with narrow band gap of 0.4 eV, thus for the same cut off wavelength, larger particles need to be grown, the latter has a quasi-spherical shape as revealed by TEM in Figure 1d. More material analysis such as X-ray diffraction and X-ray photoemission are available as Figure S1 and S2 respectively.

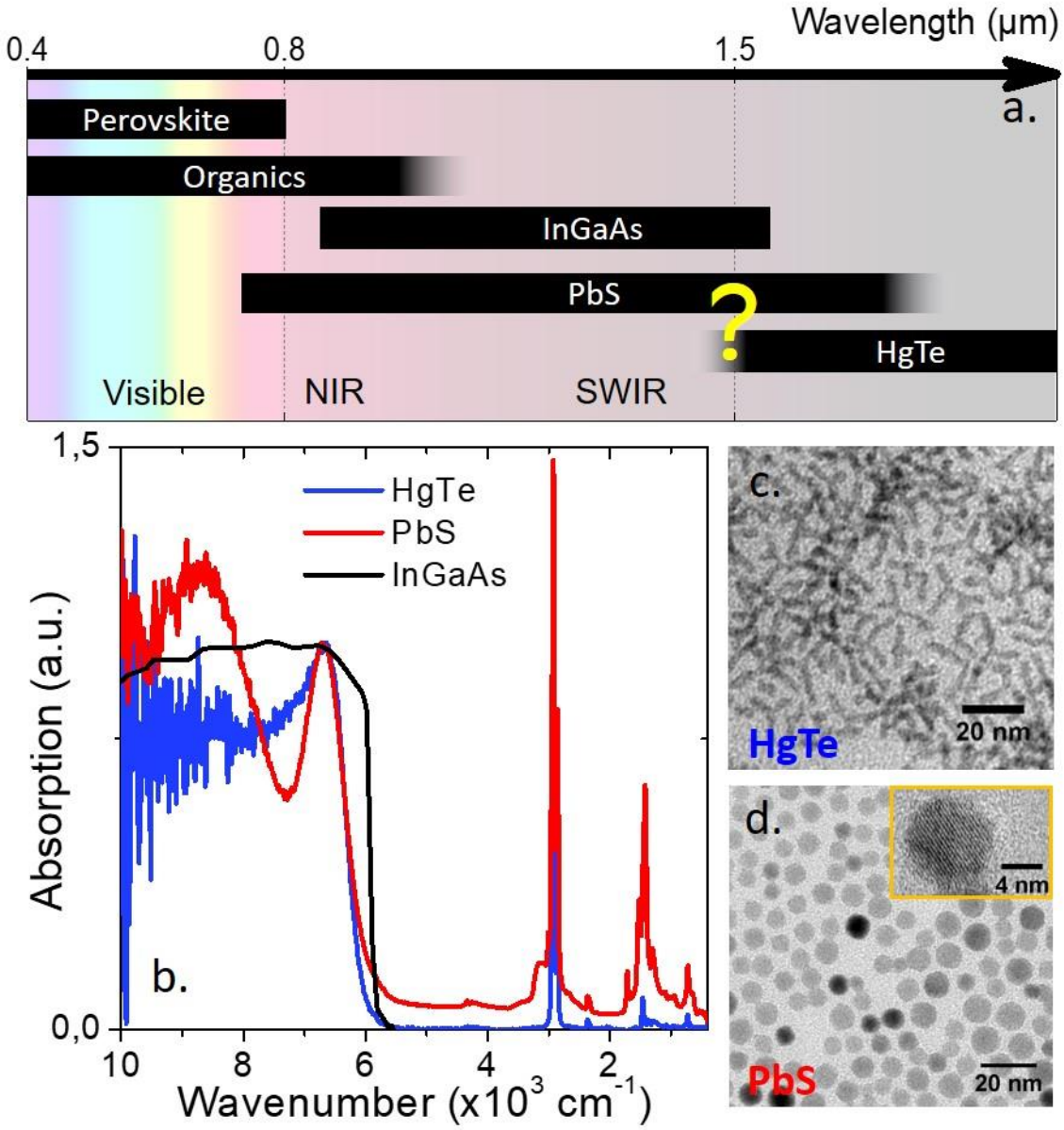

Figure 1 a. Electromagnetic spectrum in the visible and infrared ranges. The ranges achievable by several technologies (perovskite, organics, PbS nanocrystals and HgTe nanocrystals) are highlighted. b. Absorption spectrum from an InGaAs detector and from PbS (red) and HgTe (blue) nanocrystals with the same cut-off wavelength. Transmission electron microscopy image of HgTe (c.) and PbS (d.) nanocrystals with a band gap similar to InGaAs.

The transport properties are then tested as the material is deposited on interdigitated electrodes, see figure S4 for a scheme of the device. A ligand exchange step is conducted to increase the inter-nanocrystals coupling. We choose ethanedithiol as capping ligand because of its high affinity for both lead and mercury. Thanks to their narrow band gap nature, electrons can be thermally promoted to the conduction band which ensure conduction even in dark condition, see Figure 2a and d. Under illumination, with a laser source at 1.55 µm, we observe a positive photoresponse. For a thin film, which thickness is around 150 nm, and which was prepared using solid state ligand exchange toward ethanedithiol capping, the responsivity has been determined to be 3.5 mA/W and 1.1 mA/W for HgTe and PbS respectively. The two materials also present a similar temperature dependence, see Figure 2b and e. The I-Temperature curves can be fitted using an Arrhenius law with an activation energy of 150 meV and 160 meV respectively for HgTe and PbS. These values are significantly smaller than half the optical band gap value expected for an intrinsic semiconductor. This suggests that materials are doped. To reveal the nature of the majority carriers, we use an ion gel transistor configuration[39]. We notice a first striking difference between the two materials. HgTe presents a p-type nature (see Figure 2c) which means that conductance increases under hole injection (*i.e.* under negative gate bias) , while for the same capping ligands the PbS nanocrystals are n-type (see Figure 2f, conductance rises under electron injection). Note that this observation is fully consistent with the reconstructed electronic spectra of the two materials obtained by combining infrared spectroscopy and photoemission, see Figure 3f. We found that, for PbS nanocrystals, the Fermi level is resonant with the conduction band while, it lies in the bottom part of the band gap for HgTe. We have also tested the promptness of the photoresponse, both materials are able to have a fast time response. The bode diagram, see Figure 2g, reveals that the 3-dB cut off frequency is around 2 kHz for PbS and around 10 kHz for HgTe. The power dependency of the two materials reveals a fairly similar behavior with a sub linear increase of the current with the incident power, see Figure 2h.

In this geometry the two devices have quite similar detectivity in the 10^7-10^8 jones range, see figure S5 and S6. Obvious strategies to enhance the performances are (*i*) increasing the film thickness to enhance the absorption, (*ii*) reducing the incident power flux to take advantage of the non-linear response of the material with incident photon intensities and most importantly (*iii*) the design of a photovoltaic geometry to operate the device at zero volt and reduce dark current. However, conducting the comparison of the two materials in such geometry would have been unfair since performance are then driven by diode energy landscape (*i.e.* the band alignment with charge extraction layer) rather than by active material itself.

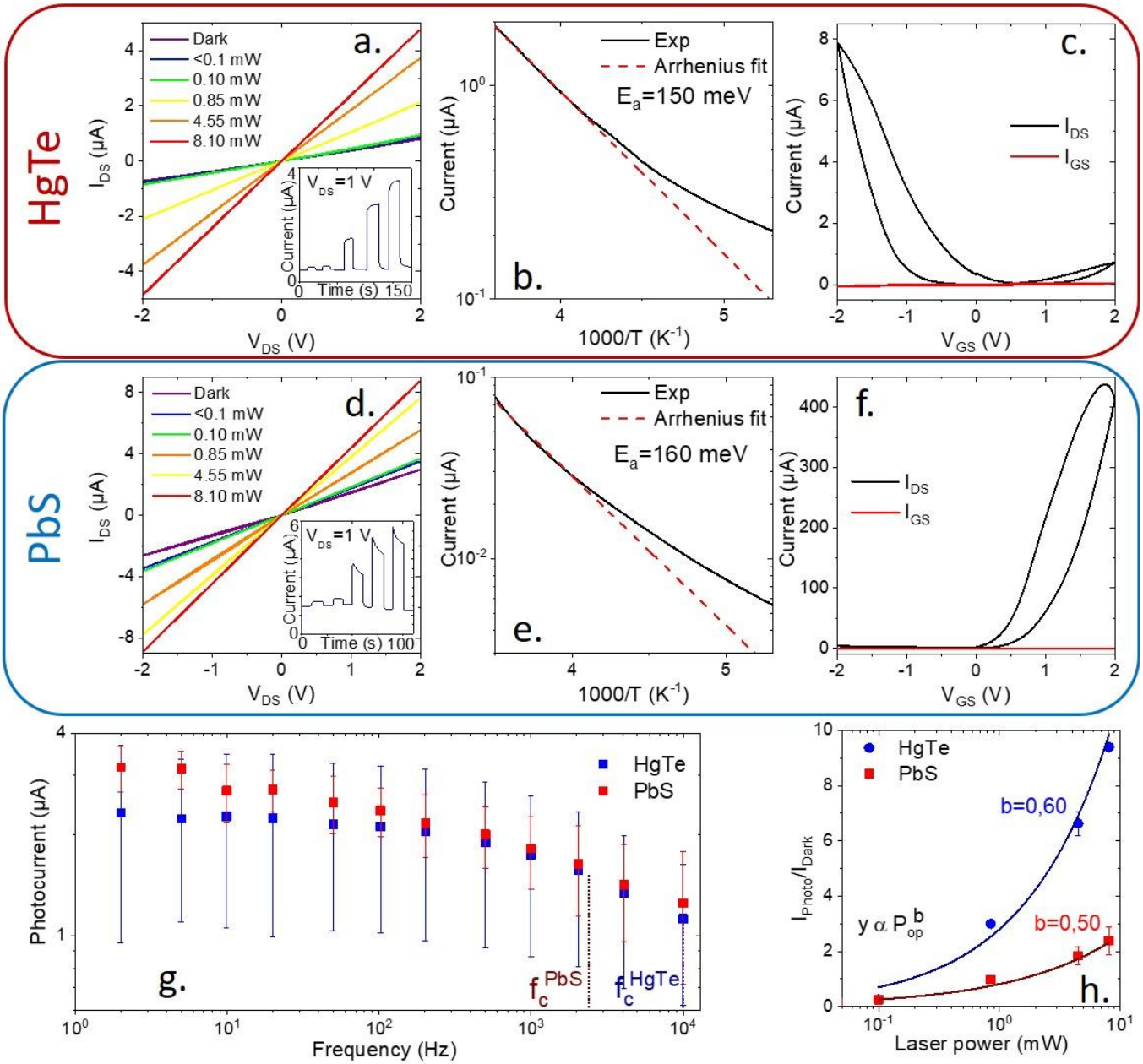

Figure 2a. Current as a function of the applied bias under dark condition and under illumination by a 1.55 µm laser for a thin film of HgTe nanocrystals. The inset is the current as a function of time while the sample is illuminated by pulses of 1.55 µm laser of various intensities. b. Current as a function of temperature for a thin film of HgTe nanocrystals capped with ethanedithiol. The high temperature part of the curve fits an Arrhenius law. c. Transfer curve (i.e. drain and gate currents as a function of the applied gate bias) for a an electrolyte gated transistor which channel is made of a thin film of HgTe nanocrystals capped with ethanedithiol. d. Current as a function of the applied bias under dark condition and under illumination by a 1.55 µm laser for a thin film of PbS nanocrystals. The inset is the current as a function of time while the sample is illuminated by pulses of 1.55 µm laser of various intensities. e. Current as a function of temperature for a thin film of PbS nanocrystals capped with ethanedithiol. The high temperature part of the curve fits an Arrhenius law. f. Transfer curve (i.e. drain and gate currents as a function of the applied gate bias) for an electrolyte gated transistor which channel is made of a thin film of PbS nanocrystals capped with ethanedithiol. g. Bode diagram (i.e. magnitude of the photocurrent as a function of frequency) for thin film of HgTe (blue) and PbS (red) nanocrystals. h. Current modulation at 1 V bias under illumination (i.e. ratio of the current under illumination over the dark current) for thin film of HgTe and PbS nanocrystals as a function of the laser illumination.

From an operational point of view, an IR detector needs to be operated in the -20 °C to 60 °C range, nanocrystals may even be exposed to higher temperature during the device fabrication. Atomic Layer Deposition (ALD) is now commonly

used as a strategy to encapsulate devices[40–42], but the latter is conducted at an intermediate temperature around 150 °C. Similarly, lithography procedure generally requires baking step at temperature above 100 °C. It becomes of utmost importance to quantize the thermal stability of the two materials. Here, we have tested how the absorption spectrum and transport properties are affected by an annealing step in the 50 to 150 °C range.

For HgTe nanocrystals, the spectrum is barely affected by low temperature (50 °C) annealing, see Figure 3a. Analysis of the Hg 4f state by photoemission does not reveals any evidence of oxidation. Two contributions are observed for Hg[43,44], which relates to Hg coupled with Te (binding energy, BE(Hg $4f_{7/2}$)=100.37 eV) in the bulk of the nanocrystal and Hg coupled with sulfur of the surface thiol BE(Hg $4f_{7/2}$)=100.9 eV, see Figure 3d. On the other hand, at higher temperatures (100 °C and more), the exciton fully disappears and is replaced by a long tail of absorption, which extends up to very long wavelengths[45]. We observe that the dark current is unchanged for low temperatures (up to 50 °C) and dramatically increases for annealing at 100 °C and more, see Figure 3c. To obtain a 1.7 µm cut-off wavelength from HgTe, small nanocrystals are grown at low temperature (55 °C). Annealing step above the growth temperature leads to a strong nanocrystal sintering, which is responsible for the dramatic broadening of the absorption. The latter also strongly affects the dark current which is exponentially dependent on the absorption tails.

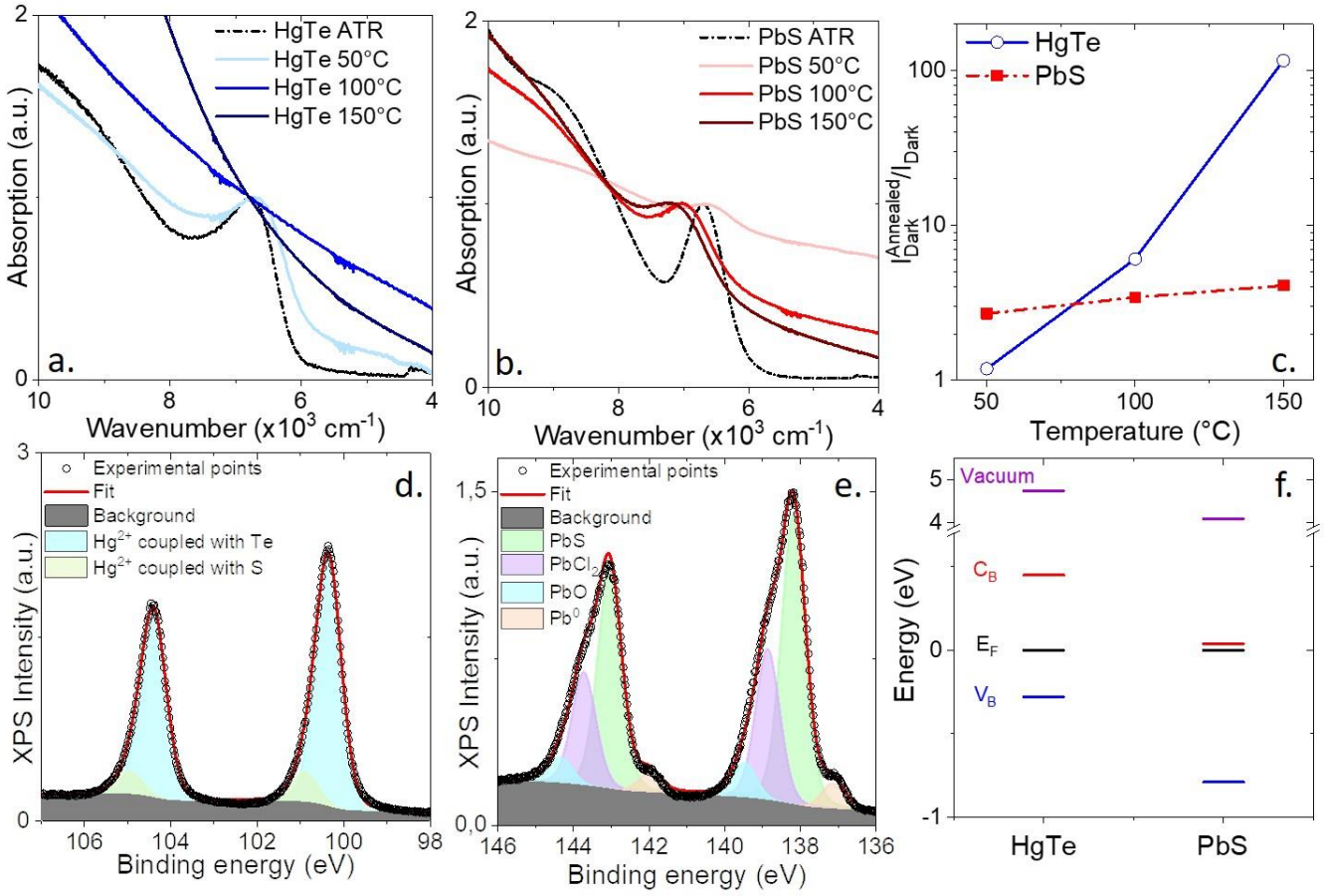

Figure 3 a. Absorption of HgTe nanocrystals in solution and under thin film form after a 15-minutes annealing at various temperatures. The annealing is made at ambient atmosphere. b. Absorption of PbS nanocrystals in solution under thin film form after and a 15-minutes annealing at various temperatures. The annealing is made at ambient atmosphere. c. Ratio of the current after and before annealing for thin film of HgTe and PbS nanocrystals as a function of the annealing temperature. The annealing is made at ambient atmosphere. d. Photoemission spectrum relative to the Hg 4f state from a thin film of HgTe nanocrystals capped with ethandithiol ligands. e. Photoemission spectrum relative to the Pb 4f state from a thin film of PbS nanocrystals capped with ethandithiol ligands. f. Energy of the valence band, conduction band and vacuum level for HgTe and PbS nanocrystals with a 1.7 µm cut-off wavelength and capped with ethanedithiol ligands. Fermi level is taken as a reference at 0 eV in both cases.

PbS nanocrystals present a different degradation mechanism with temperature. Already at 50 °C, we observe a blue shift of the absorption spectrum, see Figure 3b. This corresponds to the formation of a shell of lead oxide onto the nanocrystal surface. The latter is clearly revealed by photoemission of the Pb 4f state, see Figure 3e. The analysis of the Pb 4f states for a sample before annealing reveals four contributions at BE = 137.15 eV, 138.19 eV, 138.87 eV and 139.5 eV that are respectively attributed to lead under Pb^0, PbS, $PbCl_2$ and PbO form. The degradation mechanism for PbS is a combination of two opposite effects. At first PbS oxidizes forming a PbO shell which increases the confinement. The latter is then balanced by the nanocrystal sintering occurring at high temperature. From a transport point of view, PbS may appear more robust since the resistance is not as dramatically affected as for HgTe. However, the phototransport will be affected by the presence of the PbO shell. It is worth mentioning that with glove box processing of PbS, the oxidation process is suppressed and only the effect of the sintering (*i.e.* the broadening of the peak and the dramatic Increase of the dark current) is observed, see Figure S7. This sensitivity of SWIR nanocrystals to the exposure to high temperatures is currently a clear limitation. Different paths such as low temperature encapsulation[45] and growth of core-shell have been proposed[46] to overcome this limitation but more work will be required.

The design of efficient photodiode based on PbS has greatly benefit from the possibility to induce n and p nature to the PbS layer thanks to ligand exchange. On PbS, this effort has already been conducted[36,47,48], but these data are currently lacking for HgTe with a 1.7 µm cut off while they are of utmost interest for the design of photovoltaic devices. Using ultraviolet photoemission (Figure S3) and infrared spectroscopy (Figure 4a) , we have revealed the shift of the conduction, valence and vacuum levels with respect to the Fermi level resulting from the modification of the surface chemistry, see Figure 4b. As the long initial dodecanethiol ligands are stripped and replaced by shorter molecules we observe a systematic redshift of the band edge energy, see Figure 4a. In addition, tuning the capping ligands allows to displace the Fermi level within the band gap by 0.3 eV, which is significant for a band edge energy of 0.73 eV. Using transistor measurements, we have confirmed that the nature of the majority carriers can be significantly affected. Using thiocyanate ligands, we observe a clear ambipolar behavior, see Figure 4c, where the electron transport is more prominent than for EDT capping, see Figure 2b. Conversely, the nanocrystals capped with S^{2-}, from Na_2S, have only p-type behavior with no evidence for electron conduction, see Figure 4d.

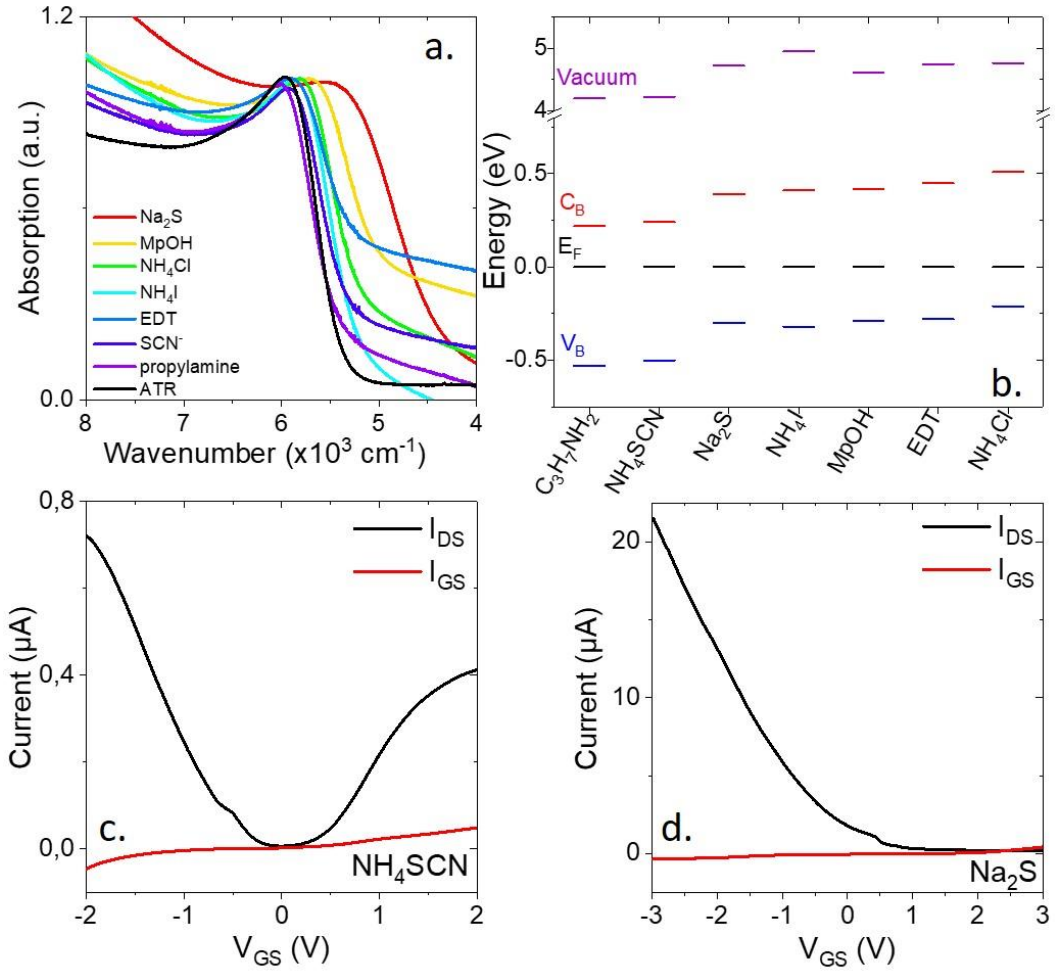

Figure 4 a. FTIR spectra for HgTe CQD film capped with different ligands. (b.)Energy of the valence band, conduction band and vacuum level for HgTe nanocrystals with a 1.7 µm cut-off wavelength and different caping ligands. The Fermi level is set at 0 eV. Transfer curve (drain and gate currents as a function of gate bias) for an electrolyte gated transistor which channel is made from a thin film of HgTe nanocrystals capped with SCN^- (c.) and S^{2-} (d.).

The last part of the paper is focused on the integration of the HgTe nanocrystals into multipixel devices. Again this effort has already been done for PbS material in the SWIR[49] and for HgTe at longer wavelengths[50,51] (*i.e.* with 5 µm cut-off) but not for HgTe around 1.7 µm cut-off. The design of such multipixel device is critical to quantize issues such as deposition inhomogeneity and spatial noise. We first use a matrix of 10x10 pixels (see Figure 5a and b) with a 30 µm pitch which was recently proposed to design infrared laser beam profiles[12]. The fabrication and the nanocrystal film deposition are described in the supporting information. The current in the device, under 0.1 V of applied bias, is quantized in Figure 5c. The mean value of the dark current is 0.4 nA. The linewidth of the dark current histogram is $\Delta I/I_{dark} \approx 0.68$. The broadening of the transition has two contributions, inhomogeneity of the electrodes and spatial fluctuation of the film conductance. To disentangle these two contributions, one can look to the linewidth of the photocurrent histogram. If the contribution of the film was prevailing, we should anticipate an increase of the linewidth width the increase of conductance under illumination. We actually observe no increase of current distribution under illumination ($\Delta I/I_{light} \approx 0.69$). We can conclude that the spatial inhomogeneity of the film (variation of thickness, presence of cracks….) is actually quite low at the scale of the matrix (300 µm). In a second step we have deposited the same material onto the surface of a proprietary VGA read out circuit from New Imaging Technologies. A cropped image (549x254 pixels) obtained with the matrix is given in Figure 5d. The white area corresponds to the signal under illumination by a laser spot at 1.55 µm. Interestingly the number of dead pixels remains extremely limited, see the right part of the image. The sensitivity of the device allows to reveal the spatial distribution of the laser beam, see Figure 5e. A video of the scene is available in supporting information (see video S1) and confirms the fast time

response of the material with a lack of memory effect. This observation further confirms the potential of nanocrystal-based sensors for the control of infrared laser beam and their alignment.

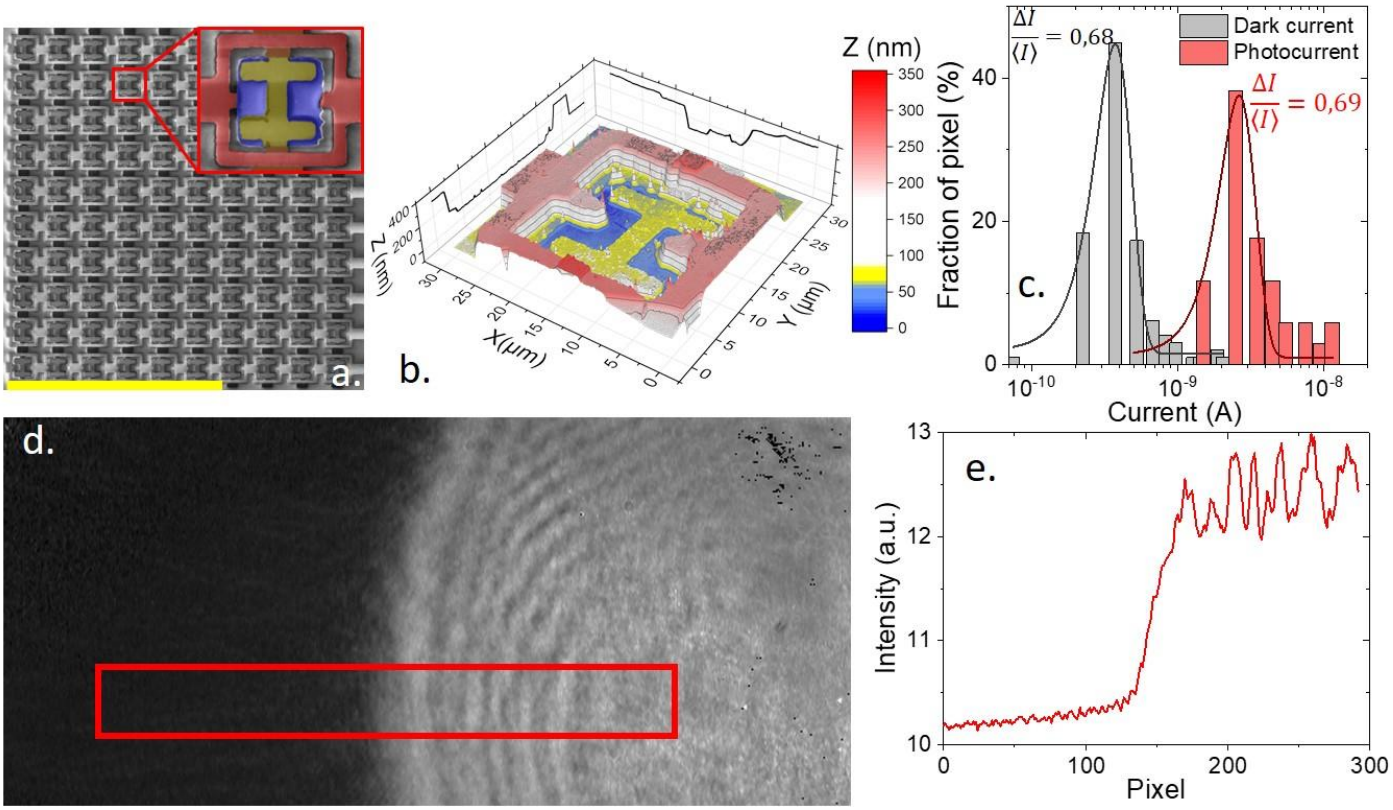

Figure 5 a. Scanning electron microscopy picture of the pixel matrix (magnification x 400). Scale bar is 200 µm. The inset is a zoom on a pixel (30 x 30 µm) in faux colors: blue is the bare substrate, yellow the bottom contact, gray the silica onto the substrate and red the top contact. b. Thickness map of a pixel. c. Histogram of the dark (gray) and the current under 1.55 µm (0.13 W.cm^{-2}) illumination (red), under 0.1 V of applied bias . A gaussian fit is applied, the mean dark current is 0.37 nA and the full width at half maximum is 0.25 nA. For the photocurrent the mean current is 2.6 nA and the FWHM is 1.8 nA. d. Image of the laser beam taken with VGA read out circuit surface. Dead pixels appear in black on the right part of the image. e. Profile of the laser beam taken in the red rectangle of the image 5d.

CONCLUSION

We have conducted a comparison of PbS and HgTe nanocrystals as a possible alternative to InGaAs material for SWIR detection. The two materials actually present similar detection properties (similar responsivity and time response) but very different aging mechanisms, with HgTe being poorly sensitive to oxidation but more strongly to sintering due to its low growth temperature. As the effort for the integration of HgTe at such wavelengths is not as strong as for PbS, we have chosen to investigate more deeply their electronic structure and especially strategy to tune the doping via ligand exchange. We reveal that the material can be tuned from p-type to ambipolar depending on the surface chemistry. HgTe nanocrystal films are finally integrated into multipixel devices which aim to be used as infrared laser beam profilers. We reveal that the film presents a good homogeneity, a low dark current (400 pA for 30 µm pixel pitch), and a low amount of dead pixels (≈1%).

MATERIALS AND METHODS

Chemicals. Mercury chloride ($HgCl_2$, Strem Chemicals, 99%), tellurium powder (Te, Sigma-Aldrich, 99.99%), trioctylphosphine (TOP, Cytek, 90%), oleylamine (Acros, 80-90%), dodecanethiol (DDT, Sigma-Aldrich, 98%), lead chloride ($PbCl_2$, Afla Aesar, 99%), sulfur powder (S, Afla Aesar, 99.5%), oleic acid (OA, Afla Aesar, 90%), 1,2,ethanedithiol (EDT, Fluka, 98.0%), lithium perchlorate ($LiClO_4$, Sigma-Aldrich, 98%), polyethylene glycol (PEG, M_w = 6 $kg.mol^{-1}$), chloroform (VWR), ethanol absolute anhydrous (VWR), methanol (Carlo Erba, 99.8%), acetone (VWR), n-hexane (VWR), n-octane (SDS, 99%), toluene (Carlo Erba, 99.3%), N,N-dimethylformamide (DMF, Sigma Aldrich), ammonium iodine (NH_4I, Alfa Aesar, ≥ 99%), mercaptoalcool (MpOH, Merck, >99%), propylamine ($C_3H_7NH_2$, Across, 99%), ammonium chloride (NH_4Cl, Sigma Aldrich, 99.998%), Sodium sulfate nanohydrate ($Na_2S,9H_2O$, Sigma Aldrich, ≥ 99.99%), ammonium thiocyanate (NH_4SCN, Sigma Aldrich, 97.5%).

All chemicals are used as received, except oleylamine which is centrifuged before use. **Mercury and lead salts are toxic, handle them with great care.**

***1 M TOP:Te precursor*.** In a three-neck flask, 2.54 g of Te powder is mixed in 20 mL of TOP. The flask is kept under vacuum at room temperature for 5 min and then is heated up to 100 °C and kept under vacuum for 20 min more. The atmosphere is changed for Ar and the temperature is raised to 275 °C. The solution is stirred until a clear orange coloration is obtained. Then the flask is cooled down and the color switches to yellow. The flask is degassed again for 10 min at room temperature. This solution is finally transferred to an Ar-filled glovebox for storage.

***HgTe CQD Synthesis*.** In a 100 mL three-neck flask, 543 mg of $HgCl_2$ and 60 mL of oleylamine (OLA) are degassed form room temperature to 110 °C for an hour. The atmosphere is then switched to Ar and the solution is cooled down to 50 °C. A solution of 2 mL of TOP:Te (1 M) and 10 mL of OLA is quickly added to the flask after warming it up with a heat gun. After 3 minutes, the reaction is quickly quenched by addition of a mixture of 2 mL of DDT and 10 mL of toluene. The nanocrystals are precipitated with ethanol and redispersed in toluene. Then the nanocrystals are precipitated with methanol and redispersed in toluene. The solution is centrifugated at is. The pellet is eliminated and the supernatant is washed one more time. Finally, the HgTe CQD solution in toluene is filtered through a 0.2 µm PTFE filter. The obtained solution is used for further characterization and device fabrication.

***PbS CQD Synthesis*.** In a three-neck flask, 300 mg of $PbCl_2$ and 7.5 mL of OLA are degassed, first at room temperature and then at 110 °C for 30 min. Meanwhile, 30 mg of S powder is mixed with 7.5 mL of OLA until full dissolution and an orange clear solution is obtained. Then under Ar at 160 °C, this solution of S is quickly added to the flask. After 15 minutes, the reaction is quickly quenched by addition of 1 mL of OA and 10 mL of hexane. The nanocrystals are precipitated with ethanol and redispersed in toluene. This washing step is repeated one more time. The solution is then centrifugated at is, to remove the unstable phase. The supernatant is precipitated with methanol and redispersed in toluene. Finally, the PbS CQD solution in toluene is filtered through a 0.2 µm PTFE filter. The obtained solution is used for further characterization and devices' fabrication.

ASSOCIATED CONTENT

Supporting Information

The Supporting Information is available free of charge on the ACS Publications web site at.

This includes material characterization using IR spectroscopy, photoemission measurements, fabrication and characterization of photoconductive device. A movie of the HgTe nanocrystal film deposited on the read-out circuit is also available. The signal corresponds to the illumination of the camera by a 1.55 µm laser.

AUTHOR INFORMATION

Corresponding Author

*E-mail: el@insp.upmc.fr (EL)

Funding

EL thanks the support ERC starting grant blackQD (grant n° 756225). We acknowledge the use of clean-room facilities from the "Centrale de Proximité Paris-Centre". This work has been supported by the Region Ile-de-France in the framework of DIM Nano-K (grant dopQD). This work was supported by French state funds managed by the ANR within the Investissements d'Avenir programme under reference ANR-11-IDEX-0004-02, and more specifically within the framework of the Cluster of Excellence MATISSE and also by the grant IPER-Nano2, Copin, Graskop, Frontal. JQ thanks Chinese Scholar council for PhD grant while AC thanks l'Agence Innovation Défense for PhD funding.

Notes

The authors declare no competing financial interest

REFERENCES

(1) Goubet, N.; Jagtap, A.; Livache, C.; Martinez, B.; Portalès, H.; Xu, X. Z.; Lobo, R. P. S. M.; Dubertret, B.; Lhuillier, E. Terahertz HgTe Nanocrystals: Beyond Confinement. *Journal of the American Chemical Society* **2018**, *140*, 5033–5036.

(2) McDonald, S. A.; Konstantatos, G.; Zhang, S.; Cyr, P. W.; Klem, E. J. D.; Levina, L.; Sargent, E. H. Solution-Processed PbS Quantum Dot Infrared Photodetectors and Photovoltaics. *Nature Materials* **2005**, *4*, 138–142.

(3) Semonin, O. E.; Luther, J. M.; Choi, S.; Chen, H.-Y.; Gao, J.; Nozik, A. J.; Beard, M. C. Peak External Photocurrent Quantum Efficiency Exceeding 100% via MEG in a Quantum Dot Solar Cell. *Science* **2011**, *334*, 1530–1533.

(4) Kershaw, S. V.; Susha, A. S.; Rogach, A. L. Narrow Bandgap Colloidal Metal Chalcogenide Quantum Dots: Synthetic Methods, Heterostructures, Assemblies, Electronic and Infrared Optical Properties. *Chem. Soc. Rev.* **2013**, *42*, 3033–3087.

(5) Lhuillier, E.; Guyot-Sionnest, P. Recent Progresses in Mid Infrared Nanocrystal Optoelectronics. *IEEE Journal of Selected Topics in Quantum Electronics* **2017**, *23*, 6000208.

(6) Kim, J.; Ouellette, O.; Voznyy, O.; Wei, M.; Choi, J.; Choi, M.-J.; Jo, J. W.; Baek, S.-W.; Fan, J.; Saidaminov, M. I.; et al. Butylamine-Catalyzed Synthesis of Nanocrystal Inks Enables Efficient Infrared CQD Solar Cells. *Advanced Materials* **2018**, *30*, 1803830.

(7) Chuang, C.-H. M.; Brown, P. R.; Bulović, V.; Bawendi, M. G. Improved Performance and Stability in Quantum Dot Solar Cells through Band Alignment Engineering. *Nat Mater* **2014**, *13*, 796–801.

(8) Im, S. H.; Kim, H.; Kim, S. W.; Kim, S.-W.; Seok, S. I. Efficient HgTe Colloidal Quantum Dot-Sensitized near-Infrared Photovoltaic Cells. *Nanoscale* **2012**, *4*, 1581–1584.

(9) Kovalenko, M. V.; Kaufmann, E.; Pachinger, D.; Roither, J.; Huber, M.; Stangl, J.; Hesser, G.; Schäffler, F.; Heiss, W. Colloidal HgTe Nanocrystals with Widely Tunable Narrow Band Gap Energies: From Telecommunications to Molecular Vibrations. *J. Am. Chem. Soc.* **2006**, *128*, 3516–3517.
(10) Chen, M.; Shao, L.; Kershaw, S. V.; Yu, H.; Wang, J.; Rogach, A. L.; Zhao, N. Photocurrent Enhancement of HgTe Quantum Dot Photodiodes by Plasmonic Gold Nanorod Structures. *ACS Nano* **2014**, *8*, 8208–8216.
(11) Chen, M.; Yu, H.; Kershaw, S. V.; Xu, H.; Gupta, S.; Hetsch, F.; Rogach, A. L.; Zhao, N. Fast, Air-Stable Infrared Photodetectors Based on Spray-Deposited Aqueous HgTe Quantum Dots. *Advanced Functional Materials* **2014**, *24*, 53–59.
(12) Martinez, B.; Ramade, J.; Livache, C.; Goubet, N.; Chu, A.; Gréboval, C.; Qu, J.; Watkins, W. L.; Becerra, L.; Dandeu, E.; et al. HgTe Nanocrystal Inks for Extended Short-Wave Infrared Detection. *Advanced Optical Materials* **2019**, 1900348.
(13) Böberl, M.; Kovalenko, M. V.; Gamerith, S.; List, E. J. W.; Heiss, W. Inkjet-Printed Nanocrystal Photodetectors Operating up to 3 Mm Wavelengths. *Advanced Materials* **2007**, *19*, 3574–3578.
(14) Chen, M.; Lu, H.; Abdelazim, N. M.; Zhu, Y.; Wang, Z.; Ren, W.; Kershaw, S. V.; Rogach, A. L.; Zhao, N. Mercury Telluride Quantum Dot Based Phototransistor Enabling High-Sensitivity Room-Temperature Photodetection at 2000 Nm. *ACS Nano* **2017**, *11*, 5614–5622.
(15) Cryer, M. E.; Halpert, J. E. 300 nm Spectral Resolution in the Mid-Infrared with Robust, High Responsivity Flexible Colloidal Quantum Dot Devices at Room Temperature. *ACS Photonics* **2018**, *5*, 3009–3015.
(16) Jagtap, A.; Martinez, B.; Goubet, N.; Chu, A.; Livache, C.; Gréboval, C.; Ramade, J.; Amelot, D.; Trousset, P.; Triboulin, A.; et al. Design of a Unipolar Barrier for a Nanocrystal-Based Short-Wave Infrared Photodiode. *ACS Photonics* **2018**, *5*, 4569–4576.
(17) Tang, X.; Ackerman, M. M.; Guyot-Sionnest, P. Thermal Imaging with Plasmon Resonance Enhanced HgTe Colloidal Quantum Dot Photovoltaic Devices. *ACS Nano* **2018**, *12*, 7362–7370.
(18) Tang, X.; Ackerman, M. M.; Chen, M.; Guyot-Sionnest, P. Dual-Band Infrared Imaging Using Stacked Colloidal Quantum Dot Photodiodes. *Nature Photonics* **2019**, *13*, 277–282.
(19) Keuleyan, S.; Lhuillier, E.; Brajuskovic, V.; Guyot-Sionnest, P. Mid-Infrared HgTe Colloidal Quantum Dot Photodetectors. *Nature Photonics* **2011**, *5*, 489–493.
(20) Hafiz, S. B.; Scimeca, M. R.; Zhao, P.; Paredes, I. J.; Sahu, A.; Ko, D.-K. Silver Selenide Colloidal Quantum Dots for Mid-Wavelength Infrared Photodetection. *ACS Appl. Nano Mater.* **2019**, *2*, 1631–1636.
(21) Tang, X.; Tang, X.; Lai, K. W. C. Scalable Fabrication of Infrared Detectors with Multispectral Photoresponse Based on Patterned Colloidal Quantum Dot Films. *ACS Photonics* **2016**, *3*, 2396–2404.
(22) Hafiz, S. B.; Scimeca, M.; Sahu, A.; Ko, D.-K. Colloidal Quantum Dots for Thermal Infrared Sensing and Imaging. *Nano Convergence* **2019**, *6, 7*.
(23) Livache, C.; Martinez, B.; Goubet, N.; Ramade, J.; Lhuillier, E. Road Map for Nanocrystal Based Infrared Photodetectors. *Front. Chem.* **2018**, *6, 575*.
(24) Tauziede, L.; Beulé, K.; Boutillier, M.; Bernard, F.; Reverchon, J.-L.; Buffaz, A. In Evaluation of InGaAS array detector suitability to space environment. *Proc. SPIE* **2017**, 10564, 105640O.
(25) Swarnkar, A.; Marshall, A. R.; Sanehira, E. M.; Chernomordik, B. D.; Moore, D. T.; Christians, J. A.; Chakrabarti, T.; Luther, J. M. Quantum Dot–Induced Phase Stabilization of α-$CsPbI_3$ Perovskite for High-Efficiency Photovoltaics. *Science* **2016**, *354*, 92–95.
(26) Protesescu, L.; Yakunin, S.; Bodnarchuk, M. I.; Krieg, F.; Caputo, R.; Hendon, C. H.; Yang, R. X.; Walsh, A.; Kovalenko, M. V. Nanocrystals of Cesium Lead Halide Perovskites ($CsPbX_3$, X = Cl, Br, and I): Novel Optoelectronic Materials Showing Bright Emission with Wide Color Gamut. *Nano Lett.* **2015**, *15*, 3692–3696.
(27) YousefiAmin, A.; Killilea, N. A.; Sytnyk, M.; Maisch, P.; Tam, K. C.; Egelhaaf, H.-J.; Langner, S.; Stubhan, T.; Brabec, C. J.; Rejek, T.; et al. Fully Printed Infrared Photodetectors from PbS Nanocrystals with Perovskite Ligands. *ACS Nano* **2019**, *13*, 2389–2397.
(28) Killilea, N.; Wu, M.; Sytnyk, M.; Amin, A. A. Y.; Mashkov, O.; Spiecker, E.; Heiss, W. Pushing PbS/Metal-Halide-Perovskite Core/Epitaxial-Ligand-Shell Nanocrystal Photodetectors beyond 3 μm Wavelength. *Advanced Functional Materials* **2019**, *29*, 1807964.
(29) Hudson, M. H.; Chen, M.; Kamysbayev, V.; Janke, E. M.; Lan, X.; Allan, G.; Delerue, C.; Lee, B.; Guyot-Sionnest, P.; Talapin, D. V. Conduction Band Fine Structure in Colloidal HgTe Quantum Dots. *ACS Nano* **2018**, *12*, 9397–9404.
(30) Cryer, M. E.; Fiedler, H.; Halpert, J. E. Photo-Electrosensitive Memristor Using Oxygen Doping in HgTe Nanocrystal Films. *ACS Appl. Mater. Interfaces* **2018**, *10*, 18927–18934.

(31) Geiregat, P.; Houtepen, A. J.; Sagar, L. K.; Infante, I.; Zapata, F.; Grigel, V.; Allan, G.; Delerue, C.; Van Thourhout, D.; Hens, Z. Continuous-Wave Infrared Optical Gain and Amplified Spontaneous Emission at Ultralow Threshold by Colloidal HgTe Quantum Dots. *Nature Materials* **2018**, *17*, 35–42.

(32) Seong, H.; Cho, K.; Kim, S. Photocurrent Characteristics of Solution-Processed HgTe Nanoparticle Thin Films under the Illumination of 1.3 Um Wavelength Light. *Semicond. Sci. Technol.* **2008**, *23*, 075011.

(33) Nam, M.; Kim, S.; Kim, S.; Jeong, S.; Kim, S.-W.; Lee, K. Near-Infrared-Sensitive Bulk Heterojunction Solar Cells Using Nanostructured Hybrid Composites of HgTe Quantum Dots and a Low-Bandgap Polymer. *Solar Energy Materials and Solar Cells* **2014**, *126*, 163–169.

(34) Jagtap, A. M.; Varade, V.; Konkena, B.; Ramesh, K. P.; Chatterjee, A.; Banerjee, A.; Pendyala, N. B.; Koteswara Rao, K. S. R. Interactions between Photoexcited NIR Emitting CdHgTe Quantum Dots and Graphene Oxide. *Journal of Applied Physics* **2016**, *119*, 074306.

(35) Chen, L.; Gong, H.; Wei, H.; Hu, X.; Xu, H.; Liu, P.; Cao, B. Aqueous Synthesis of CdTe and HgCdTe Quantum Dots and Their Application in Quantum Dot-Sensitized Solar Cells. *Science of Advanced Materials* **2012**, *4*, 337–341.

(36) Brown, P. R.; Kim, D.; Lunt, R. R.; Zhao, N.; Bawendi, M. G.; Grossman, J. C.; Bulović, V. Energy Level Modification in Lead Sulfide Quantum Dot Thin Films through Ligand Exchange. *ACS Nano* **2014**, *8*, 5863–5872.

(37) Keuleyan, S.; Lhuillier, E.; Guyot-Sionnest, P. Synthesis of Colloidal HgTe Quantum Dots for Narrow Mid-IR Emission and Detection. *J. Am. Chem. Soc.* **2011**, *133*, 16422–16424.

(38) Moreels, I.; Lambert, K.; Smeets, D.; De Muynck, D.; Nollet, T.; Martins, J. C.; Vanhaecke, F.; Vantomme, A.; Delerue, C.; Allan, G.; et al. Size-Dependent Optical Properties of Colloidal PbS Quantum Dots. *ACS Nano* **2009**, *3*, 3023–3030.

(39) Lhuillier, E.; Ithurria, S.; Descamps-Mandine, A.; Douillard, T.; Castaing, R.; Xu, X. Z.; Taberna, P.-L.; Simon, P.; Aubin, H.; Dubertret, B. Investigating the N- and p-Type Electrolytic Charging of Colloidal Nanoplatelets. *J. Phys. Chem. C* **2015**, *119*, 21795–21799.

(40) Devloo-Casier, K.; Geiregat, P.; Ludwig, K. F.; van Stiphout, K.; Vantomme, A.; Hens, Z.; Detavernier, C.; Dendooven, J. A Case Study of ALD Encapsulation of Quantum Dots: Embedding Supported CdSe/CdS/ZnS Quantum Dots in a ZnO Matrix. *J. Phys. Chem. C* **2016**, *120*, 18039–18045.

(41) Lambert, K.; Dendooven, J.; Detavernier, C.; Hens, Z. Embedding Quantum Dot Monolayers in Al2O3 Using Atomic Layer Deposition. *Chem. Mater.* **2011**, *23*, 126–128.

(42) Liu, Y.; Tolentino, J.; Gibbs, M.; Ihly, R.; Perkins, C. L.; Liu, Y.; Crawford, N.; Hemminger, J. C.; Law, M. PbSe Quantum Dot Field-Effect Transistors with Air-Stable Electron Mobilities above 7 $Cm^2\ V^{-1}\ s^{-1}$. *Nano Lett.* **2013**, *13*, 1578–1587.

(43) Livache, C.; Izquierdo, E.; Martinez, B.; Dufour, M.; Pierucci, D.; Keuleyan, S.; Cruguel, H.; Becerra, L.; Fave, J. L.; Aubin, H.; et al. Charge Dynamics and Optolectronic Properties in HgTe Colloidal Quantum Wells. *Nano Lett.* **2017**, *17*, 4067–4074.

(44) Martinez, B.; Livache, C.; Notemgnou Mouafo, L. D.; Goubet, N.; Keuleyan, S.; Cruguel, H.; Ithurria, S.; Aubin, H.; Ouerghi, A.; Doudin, B.; et al. HgSe Self-Doped Nanocrystals as a Platform to Investigate the Effects of Vanishing Confinement. *ACS Applied Materials & Interfaces* **2017**, *9*, 36173–36180.

(45) Jagtap, A.; Goubet, N.; Livache, C.; Chu, A.; Martinez, B.; Gréboval, C.; Qu, J.; Dandeu, E.; Becerra, L.; Witkowski, N.; et al. Short Wave Infrared Devices Based on HgTe Nanocrystals with Air Stable Performances. *J. Phys. Chem. C* **2018**, *122*, 14979–14985.

(46) Shen, G.; Guyot-Sionnest, P. HgTe/CdTe and HgSe/CdX (X = S, Se, and Te) Core/Shell Mid-Infrared Quantum Dots. *Chem. Mater.* **2019**, *31*, 286–293.

(47) Kroupa, D. M.; Vörös, M.; Brawand, N. P.; McNichols, B. W.; Miller, E. M.; Gu, J.; Nozik, A. J.; Sellinger, A.; Galli, G.; Beard, M. C. Tuning Colloidal Quantum Dot Band Edge Positions through Solution-Phase Surface Chemistry Modification. *Nature Communications* **2017**, *8*, 15257.

(48) Ganesan, A. A.; Houtepen, A. J.; Crisp, R. W. Quantum Dot Solar Cells: Small Beginnings Have Large Impacts. *Applied Sciences* **2018**, *8*, 1867.

(49) Rauch, T.; Böberl, M.; Tedde, S. F.; Fürst, J.; Kovalenko, M. V.; Hesser, G.; Lemmer, U.; Heiss, W.; Hayden, O. Near-Infrared Imaging with Quantum-Dot-Sensitized Organic Photodiodes. *Nature Photonics* **2009**, *3*, 332–336.

(50) Ciani, A. J.; Pimpinella, R. E.; Grein, C. H.; Guyot-Sionnest, P. Colloidal quantum dots for low-cost MWIR imaging. *Proc. SPIE* **2016**, 9819, 981919–981928.

(51) Buurma, C.; Pimpinella, R. E.; Ciani, A. J.; Feldman, J. S.; Grein, C. H.; Guyot-Sionnest, P. MWIR imaging with low cost colloidal quantum dot films. Proc. SPIE **2016**, 9933, 993303–993310.

TOC graphic

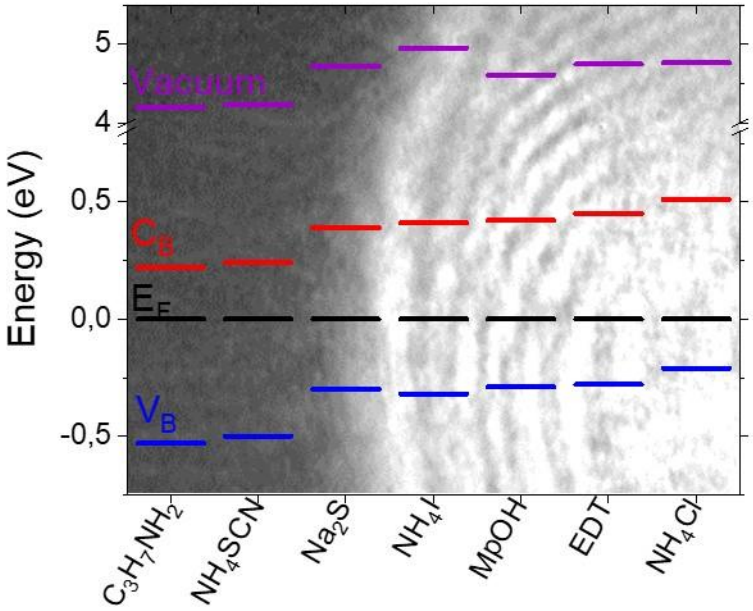
Energy (eV)
5
4
0,5
0,0
-0,5
Vacuum
C_B
E_F
V_B
$C_3H_7NH_2$
NH_4SCN
Na_2S
NH_4I
MpOH
EDT
NH_4Cl